

Validation of contact mechanics models for Atomic Force Microscopy via Finite Elements Analysis

L. Dal Fabbro, H. Holuigue, M. Chighizola* and A. Podestà*

Dipartimento di Fisica "Aldo Pontremoli" and CIMaINa, Università degli Studi di Milano,
via G. Celoria 16, 20133, Milano, Italy.

*Corresponding authors. E-mail: matteo.chighizola@unimi.it, alessandro.podesta@unimi.it

ABSTRACT

In this work, we have validated the application of Hertzian contact mechanics models and corrections in the framework of linear elasticity for the analysis of force vs indentation curves acquired using spherical indenters by means of finite elements simulations. We have systematically investigated the impact of both large indentations and vertical spatial confinement (bottom effect) on the accuracy of the nanomechanical analysis performed with the Hertz model for the parabolic indenter compared to the Sneddon model for the spherical indenter. We carried out a comprehensive characterization of the corrections for the Hertz model proposed in the literature in the framework of linearized force vs indentation curves, as well as a validation of a linearized form of the Sneddon model for the spherical indenter and of the combined correction for large indentations and bottom effect. Our results show that the corrected Hertz model in combination with the use of a spherical indenter allows to accurately quantify the Young's modulus of elasticity of linearly elastic samples and represent a powerful toolkit to analyse experimental data acquired using micrometre-sized colloidal probes on samples with variable thickness at arbitrarily large indentations.

1. INTRODUCTION

The micro- and nanoscale characterisation of the mechanical properties of systems and device components is of increasing importance in several fields like biology, where the elastic properties of cells, tissues, and extracellular matrix (ECM) can affect the behaviour and fate of an organ¹⁻⁶, or medical engineering, where microdevices with specific elastic properties are employed^{7,8}.

Atomic Force Microscopy (AFM) is an ideal tool for the quantitative and non-destructive characterisation of the mechanical properties of biological and non-biological samples at the sub-micrometer scale⁹⁻¹¹, thanks to the high spatial and force resolution of, its versatility, including the ability to work in physiological solution and controlled environments, the freedom of choosing the best tip dimensions and geometry to match the typical length scales of the system under investigation¹²⁻¹⁴.

While sharp AFM tips are mandatory when high spatial resolution is necessary, spherical probes (colloidal probes, CPs) possess several characteristics that make them suitable for the investigation of mechanical properties of soft or biological samples¹⁴. Indeed, a well-defined interaction geometry (sphere on flat, sphere on sphere) and reduced stress and strain in mechanical tests make the application of contact mechanics models more reliable, and the interpretation of results less ambiguous; the selection of the tip radius to match the characteristic length scales of the system under investigation provides better averaging of the mechanical signals together with a system-adapted spatial resolution^{13,15}.

A simple contact mechanics model describing the deformation of elastic solids was proposed by Heinrich Hertz in 1882^{16,17}. The Hertz model can be used to describe the indentation of a purely elastic, semi-infinite half space under the pressure exerted by a paraboloidal indenter. It is well known that the application of the Hertz model to real systems is based on a series of assumptions and, in some cases, gross approximations: the sample must be uniform and isotropic; interfacial adhesion must be absent; the strain and stress must be sufficiently small to ensure a linear elastic response; the sample must not exhibit a constrained mechanical response due to its spatial confinement and/or finite dimensions (the Bottom Effect problem¹⁸⁻²¹). In addition, to apply the Hertz model to data collected using spherical indenters, the indentation δ of the probe must be small compared to the radius R of the tip ($\delta \ll R$), otherwise the parabolic approximation of the spherical profile will be inaccurate (the Large Indentation problem^{22,23}).

Microscopic systems like single cells or thin tissue slices for histological analysis make the assumptions behind the use of the Hertz model to fit nanoindentation data hard to be respected. Cell height usually varies between 5-15 μm and its internal structure is extremely heterogeneous in all three dimensions, forcing to indent up to a few microns to characterise the overall mechanical response, and not just the elastic contribution of the cell membrane coupled to the actin cytoskeleton^{15,24}.

Achieving large indentions up to a few microns is even more critical for tissue or tissue-derived samples. Indeed, these samples are usually far more heterogeneous than cellular systems, across a broader range of length scales (from 50 nm to 50 μm), which requires probing a larger volume with the indenter. In addition, their surface may present micron-scale roughness due to the above-mentioned structural complexity and to the slicing process, which produces irregular interfaces, due to cell detachment and disentangled ECM fibres.

Excluding nonlinear effects, the consideration of which goes beyond the aims of the present work, the requirement of achieving large indentations on cells and other finite-thickness systems (including thin tissues or ECM slices) exposes to the risk of having both, the large indentation, and the bottom effect issues, affecting the force vs indentation curves, and impacting on the accuracy of the Hertzian analysis.

To mitigate the large indentation issue in the framework of the Hertz model, it is possible to increase the radius R of the tip to reduce the δ/R ratio; this measure however can limit the maximum indentation achievable or force to use very rigid cantilevers, with consequent loss of force sensitivity, beside causing a severe loss of spatial resolution. Alternatively, the model developed by Sneddon to describe the indentation of an elastic half-space by a spherical indenter²⁵ can be used; this model (hereafter simply called the Sneddon model) does not suffer from the constraint $\delta \ll R$. Unfortunately, Sneddon's equation for the contact radius of the spherical probe cannot be cast in an analytic close form but requires numerical methods to be solved (see section 2.2). Mitigation of the bottom effect typically requires limitation of the maximum indentation to a small fraction (well below 1/10) of the sample thickness, or height, which may keep from sensing the elastic contributions of the deeper layers of the system under investigation.

To overcome the above-mentioned limitations of the Hertz theory, the Bottom Effect Correction (BEC)^{18-20,26} and the Large Indentation Correction (LIC)^{22,23} have been proposed. The aim of such corrections is to extend the applicability of the Hertz model for the paraboloidal indenter to those cases where the estimation of the Young's modulus (YM) is biased due to the bottom effect and the large indentations, respectively.

Despite the increasing occurrence of application of BEC and LIC in published reports, a systematic validation and a suitable integration of both correction methods in a single experimental and data analysis approach are still missing. This is also due to the difficulty in producing suitable test samples for the nanomechanical investigation allowing to probe the influence of the varying thickness, spanning the range from the strong spatial confinement to the bulk conditions. The scarce availability of reference samples for nanomechanical tests limits the standardisation of the experimental and data analysis protocols^{27,28}.

In this work we present a systematic characterisation of the validity of Hertz and Sneddon models for colloidal probes based on Finite Element Analysis (FEA). FEA is a suitable tool for the simulation of the mechanical response of materials subject to the stress applied by an indenter under controlled conditions^{26,29–32}. We have used FEA to simulate force vs indentation curves on ideal elastic samples^{29,30}. We here discuss the accuracy of the Hertz model^{33,34} compared to the Sneddon model for the spherical indenter, both in bulk systems and in conditions of vertical spatial confinement and assess the accuracy of the existing large indentation and bottom effect corrections for the Hertz model. We present a simplified linearised version of the Sneddon model, which can be implemented efficiently in the same data analysis framework we developed for the use of the linearised Hertz model. Eventually, we demonstrate that LIC and BEC can be coupled in a single correction function for the Hertz model.

2. THEORETICAL MODELS AND CORRECTIONS

We present here a concise summary of the theoretical models used in this work, under the assumption of linear elasticity. For a deeper presentation and discussion of contact mechanics models, the reader is referred to some recent review papers, see Refs^{17,35}

2.1. Hertz model

The Hertz model describes the non-adhesive contact between two uniform, isotropic elastic bodies, within the framework of linear elasticity (small strain and stress), thus considering the deformations small compared to the dimensions of the bodies³⁶. Originally developed for describing the elastic contact between two spherical bodies¹⁶, the Hertz model strictly applies to the case of a paraboloidal indenter. It can be used to describe indentation by a spherical indenter provided the indentation is small compared to the tip radius ($\delta \ll R$); in this case the parabolic profile represents a

fairly accurate approximation of the circular one. In the case of indentation by an infinitely rigid paraboloid of an elastic half space with Young's modulus E and Poisson's ratio ν , the relation between the applied force F_{Hertz} and the indentation δ is:

$$F_{Hertz} = \frac{4}{3} \frac{E}{1-\nu^2} \sqrt{R} \delta^{3/2} \quad (1)$$

where R is the radius of curvature of the indenter, identified in apical region of the tip. The contact region has circular cross section, and a simple relation links the tip radius R , the indentation δ and the contact radius a (Figure S1):

$$\delta = \frac{a^2}{R}. \quad (2)$$

From Eq. 2 it follows: $a = \sqrt{\delta R}$.

2.2. Sneddon model for the spherical indenter

Sneddon developed a solution³⁷ for the case of the non-adhesive indentation of an elastic half-space by a rigid spherical indenter, represented by the system of Eqs. (3) and (4):

$$F_{Sneddon} = \frac{E}{2(1-\nu^2)} \left[(a^2 + R^2) \ln \left(\frac{R+a}{R-a} \right) - 2aR \right] \quad (3)$$

$$\delta = \frac{1}{2} a \ln \left(\frac{R+a}{R-a} \right) \quad (4)$$

The Sneddon model is not subject to the limitation $\delta \ll R$. The drawback of this model is the lack of an analytical solution linking the force to the indentation, since Eq. (4) cannot be inverted analytically to obtain the relation $a = a(\delta)$; hence, a numerical solution is required. It is worth noting that Eq. 2, valid for the Hertzian contact, represents the limit of Eq. (4) when $a/R \rightarrow 0$, which justifies the use of the simpler Hertz model when using a spherical indenter as long as the indentation δ is (very) small compared to the radius R (see Figure S1).

2.3. Large indentation corrections for the Hertz model

The Hertz model is simple (analytic and linearizable, see below), and it is therefore desirable to use it to fit indentation data obtained with spherical indenters and arbitrarily large indentations, typically up to $\delta = R$. To this purpose, in this work we have used two different corrections, proposed by Kontomaris *et al.*²² and by Muller *et al.*²³. Both correction functions $1/\Omega_{K/M}$ depend on the

nondimensional ratio $\gamma_R(\delta) = \delta/R$ and transform the experimentally measured force-indentation curve F into an apparent Hertzian curve F_{Hertz} (Eq. (1)), which can be fitted by the Hertz model across the whole range of indentations:

$$F_{Hertz}(\delta) = \frac{F(\delta)}{\Omega_{K/M}(\gamma_R(\delta))} \quad (5)$$

The function Ω_K developed by Kontomaris *et al.*²² is a power series in γ :

$$\Omega_K = c_1 + \sum_{k=2}^6 \frac{3}{2k} c_k \gamma^{k-\frac{3}{2}} \quad (6)$$

, with coefficients:

$$\begin{aligned} c_1 &= 1.0100000 \\ c_2 &= -0.0730300 \\ c_3 &= -0.1357000 \\ c_4 &= 0.0359800 \\ c_5 &= -0.0040240 \\ c_6 &= 0.0001653 \end{aligned}$$

The function Ω_M developed by Muller *et al.*²³ is a polynomial in γ :

$$\Omega_M = 1 - \frac{1}{10} \gamma - \frac{1}{840} \gamma^2 + \frac{11}{15120} \gamma^3 + \frac{1357}{6652800} \gamma^4 \quad (7)$$

Both correction functions act pointwise on the force curve, since their values depend on the indentation through the ratio γ (see Figure S2a).

2.4. Bottom effect corrections for the Hertz model

The presence of a rigid substrate underneath the sample represents a boundary condition, which, in the case of a large indentation to thickness ratio, can cause strong perturbation of strain and stress fields and therefore influence the measured elastic modulus^{17,27}. The bottom effect is a special case of the more general case of three-dimensional spatial confinement of the elastic body, where the strain and stress fields are constrained also laterally³⁸. This could be relevant, for example, when cells are at confluence, tightly arranged within a nearly two-dimensional monolayer, and firmly connected through cadherin bonds. Two correction functions for the bottom effect, $1/\Delta_{D/G}$, by Dimitriadis *et al.*¹⁸ and by Garcia *et al.*¹⁹, respectively (Figure S2b), have been developed for the paraboloidal indenter, in the case of linear elastic response, and considered in this work. The correction developed by Long

et al²⁶, which takes into account the vertical confinement for a non-linear neo-hookean material, has not been investigated in this work. These corrections can be applied, similarly to the large indentation case, to transform the experimentally measured force-indentation curve $F(\delta)$ into an apparent Hertzian curve $F_{Hertz}(\delta)$, describing the case of an infinitely extended elastic half space across the whole range of indentations:

$$F_{Hertz}(\delta) = \frac{F(\delta)}{\Delta_{D/G}(\chi_{R,h}(\delta))} \quad (8)$$

The functions developed by Dimitriadis *et al.*¹⁸ for a paraboloidal indenter refers to the following cases: i) a sample bonded to the rigid substrate (Δ_D^{bonded}); ii) a sample that is allowed to slide over it ($\Delta_D^{unbonded}$); iii) a sample that is partially bonded to the substrates (Δ_D^{cell} , like for single cells¹³):

$$\Delta_D^{bonded} = 1 + 1.133\chi + 1.283\chi^2 + 0.769\chi^3 + 0.0975\chi^4 \quad (9)$$

$$\Delta_D^{unbonded} = 1 + 0.884\chi + 0.781\chi^2 + 0.386\chi^3 + 0.0048\chi^4 \quad (10)$$

$$\Delta_D^{cell} = 1 + 1.009\chi + 1.032\chi^2 + 0.578\chi^3 + 0.051\chi^4 \quad (11)$$

Here, the driving nondimensional parameter is $\chi_{R,h}(\delta) = \frac{\sqrt{R\delta}}{h}$, where h is the height (or thickness) of the sample measured with respect to the hard substrate. The parameter χ represents the ratio between the Hertzian contact radius a (see Eq. 2) and the sample height h , which suggests that bottom effects are negligible in the limit $a \ll h$ (like for sharp probes, even though a higher stress would be produced). Noticeably, bottom effect depends on the ratio of horizontal (a) to vertical (h) dimensions, and not simply on δ/h , which in turn reminds us that the elastic deformation of a body is a truly three-dimensional process. Moreover, this also suggests that large spherical tips are more prone to bottom effects than sharp pyramidal ones.

The function Δ_G developed by Garcia *et al.*¹⁹ for a paraboloidal indenter on a sample bonded to the rigid substrate is:

$$\Delta_G = 1 + 1.133\chi + 1.497\chi^2 + 1.469\chi^3 + 0.755\chi^4 \quad (12)$$

It is worth noting that the BECs rely on the assumption of incompressibility of the sample, thus imposing a Poisson's ratio $\nu = 0.5$.

3. MATERIALS AND METHODS

3.1 Finite Elements Analysis

Finite elements simulations were performed using ANSYS Mechanical (ANSYS Student), the free version of ANSYS software, to produce ideal force vs indentation curves describing the mechanical response of elastic films in different regimes of spatial confinement, i.e., with different δ/R and $\sqrt{\delta R}/h$ ratios. The large indentations option, which retains the quadratic terms in the deformation tensor³⁹, was used in the simulations, to secure convergence. The resulting material shows, within the mesh-related error, ideal elastic behaviour across the whole tested indentation range, for both bulk and thin film configurations, as witnessed by the linearity of the effective strain vs effective stress figures of merit (according to Tabor's definition³⁰, see Figure S3).

We took advantage of the axial symmetry of the system, which allowed to create two-dimensional meshes and take full advantage of the reduced number of nodes available ($N_{\max} = 1.28 \cdot 10^5$). Simulated FCs were processed using the Hertz model with LIC and BEC and the Sneddon model for the spherical indenter. The simulated systems consist of a rigid spherical or paraboloidal tip with radius $R = 5 \mu m$ indenting an elastic medium of width $24R$ (following Ref. ^{29,31}) and two different thicknesses, to simulate both the bulk and the thin film regime. The lateral dimension of the simulated system is considered large enough to neglect spatial confinement-related effects³⁸. Three models in total were studied (see Table 1): Bulk-Sphere (B-S), Bulk-Paraboloid (B-P) and Thin Film-Sphere (TF-S); the first two models mimic the indentation of an infinite elastic half space by a spherical and a paraboloidal indenter, respectively, whereas the latter model mimics the bottom effect in case of a spherical indenter. The material was simulated with nominal Young's modulus $E_{nom} = 0.5 MPa$, Poisson's ratio $\nu = 0.49$. The choice of $\nu = 0.49$ was made to simulate a nearly incompressible material⁴⁰ (the case $\nu = 0.5$ cannot be simulated). In all models the media is bonded to a rigid substrate.

The **B-S model** consists of a rigid spherical tip of radius $R = 5 \mu m$, which indents a simulated sample with thickness $h_{bulk} = 100R$. This model was used to investigate the large indentation effect. No bottom effect is expected.

The **B-P model** consists of a rigid paraboloidal tip of radius $R = 5 \mu m$. The height of the indented simulated sample is $h_{bulk} = 100R$. This model was used to investigate the large indentation effect large indentation effect. No bottom effect is expected.

The **TF-S model** consists of a rigid spherical probe of radius $R = 5 \mu m$ which indents a simulated sample with thickness $h_{thin} = 2R$. This model was used to investigate both large indentations and bottom effects.

Representative simulated FCs are shown in Figure 3. The maximum indentation in all the cases shown in Figure 3 was $\delta = 3 \mu m$. It is possible to observe the good agreement with the theoretical models in all three configurations (Figure 1a-c). Moreover, the impact of the indenter geometry and of the spatial confinement is negligible if the δ/R ratio is below 0.2. For larger δ/R values, irrespective to the indenter geometry, the bottom effect becomes dominant; it is evident that it is necessary to apply much higher forces to indent of the same amount a spatially confined material (compare TF-S with B-S and B-P). The Sneddon and the Hertz models represent the reference contact mechanics models to describe the indentation of an elastic half-space by spherical and parabolic indenters (B-S and B-P systems, respectively), irrespective to the value of the maximum indentation.

Comparing B-S and B-P systems, it can be noticed that when indentation increases, the force needed to obtain the same indentation with the parabolic indenter increases; this is due the difference in the contact area (see Figure S1). Indeed, the parabolic contact area grows faster than the spherical one. The discrepancy between the simulated TF-S FC and the Hertzian FC corrected for the bottom effect is caused by the fact that the Hertz model is exact for the parabolic indenter, while the simulated curve assumed a spherical indenter. A suitable application of the large indentation correction is supposed to correct further this discrepancy (we will discuss this in Section 4.1.2).

<u>Model name</u>	Tip shape	Tip Radius [μm]	Sample thickness	Sample width	YM [MPa]	Poisson's ratio	Corrections to the Hertz model
B-S (Bulk-Sphere)	Sphere	5	100R	24R	0.5	0.49	LIC
B-P (Bulk-Paraboloid)	Paraboloid	5	100R	24R	0.5	0.49	None
TF-S (Thin Film-Sphere)	Sphere	5	2R	24R	0.5	0.49	BEC, LIC, BEC+LIC

Table 1. Summary of the different systems simulated for this study.

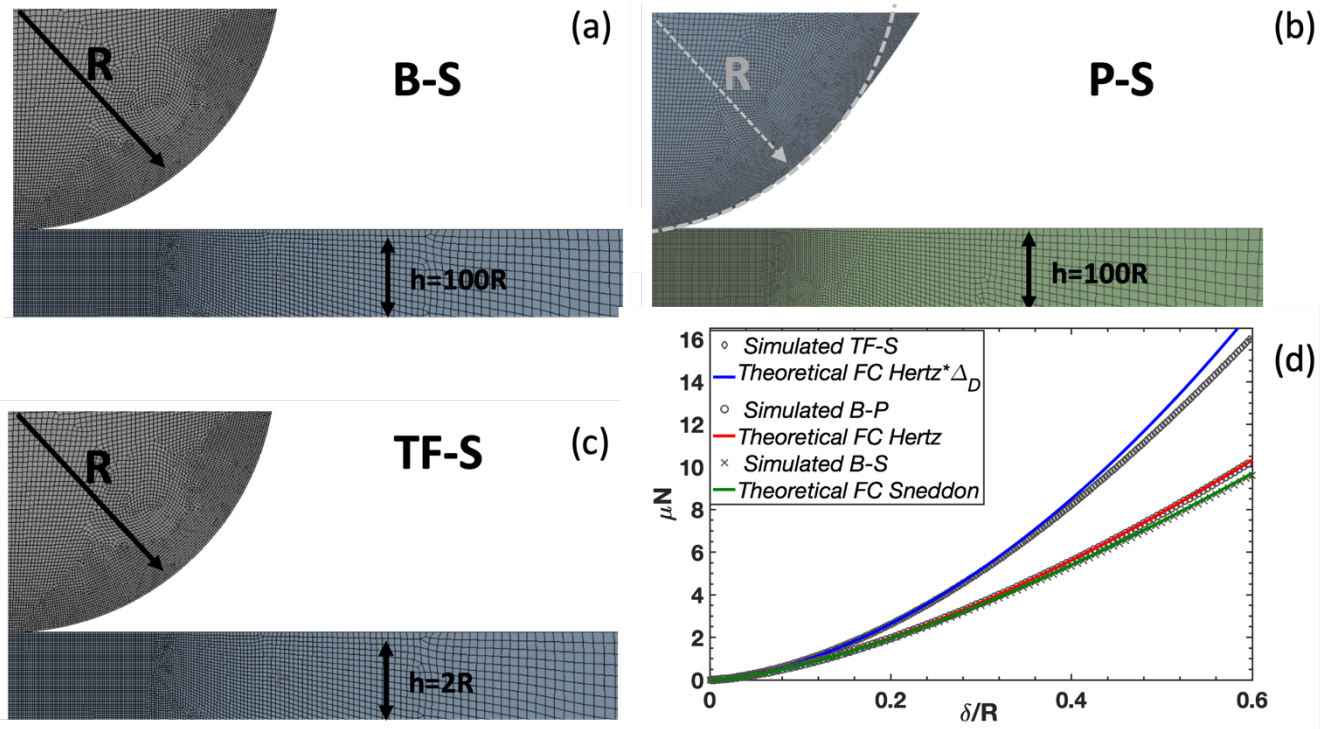


Figure 1. Representation of the different simulated configuration. (a) Spherical indenter on the bulk sample (B-S). (b) Parabolic indenter on the bulk sample (B-P). (c) Spherical indenter on the thin film sample (TF-S; $\chi=0.33$). (d) Comparison of FCs simulated using FEA for the different systems and the different theoretical FCs created from the model.

3.1.1 Mesh Optimisation

The proximity of the indenter-sample contact interface was finely meshed, and a coarser mesh was used moving away from it. Depending on indentation range, elements up to a minimum size of $0.035 \mu m$ were used.

To optimise the mesh, we studied how the number of nodes affects the measured Young's modulus E obtained through a Hertzian fit when a rigid sphere indents a sample sufficiently thick to avoid the bottom effect.

Figure S4 shows that increasing the number of nodes above $N = 2 \cdot 10^4$ has a negligible impact on the value of the YM determined by extending the fit to increasingly wider ranges of indentation. Given that the computation time for carrying out a typical simulation on a desktop PC was below 60 minutes, we decided to use the maximum number of nodes allowed ($N_{\max} = 1.28 \cdot 10^5$) within a given mesh configuration.

3.2. Data analysis

3.2.1. Hertz model

Linearizing the experimental force vs indentation curves and the Hertz model (Eq. (1)) would allow to apply a simple linear regression to the data to extract the Young's modulus. However, both measured force and indentation values (F' , δ') are typically shifted with respect to the true values (F , δ) in Eq. 1. In terms of the measured quantities, the Hertz equation is:

$$F' - F_0 = \frac{4}{3} \frac{E}{1-\nu^2} \sqrt{R} (\delta' - \delta_0)^{3/2} \quad (13)$$

In the case of the force, as long as adhesion is negligible (in principle, the Hertz model assumes no adhesion at all; when measuring in liquid, adhesion is typically very small, as the Van der Waals interactions are effectively screened by water), the offset F_0 is due in general to a misalignment of the optical beam deflection system and can be easily subtracted during the pre-processing of the raw force curves. We will assume in the following that the offset on the force axis is not present, i.e. $F'=F$.

On the other hand, an apparent indentation $\delta' = \delta + \delta_0$ is computed when rescaling the distance axis in the raw force curve, where δ_0 represents the unknown location of the contact point; δ_0 must be therefore considered as a free parameter of the fit, as well as the Young's modulus. The presence of the offset δ_0 in Eq. 13 does not allow to linearise the equation by taking the logarithm of both sides. Following Refs.^{13,41}, we adopt a convenient way to linearise Eq. 13 through the variable transformation $F^* = F^{2/3}$, which leads to the equation:

$$\delta' = \alpha F^* + \delta_0 \quad (14)$$

where the parameter α depends on the Young's modulus E :

$$\alpha = \left(\frac{3}{4} \frac{1-\nu^2}{E\sqrt{R}} \right)^{\frac{2}{3}} \quad (15)$$

and Eq. (14) holds for $\delta > \delta_0$.

The contact point δ_0 represents the intercept of the δ' vs F^* curve, while the Young's modulus E can be calculated from the slope α , since both radius R and Poisson's ratio ν are supposed to be known. The free parameters of the fit, δ_0 and E , are not correlated in Eq. 14, and can therefore be determined independently; this is not the case in the original Hertz model (Eq. 1).

To precisely identify the position where the probe gets in contact with the sample, we used the protocol described in detail by Puricelli et al.¹³. δ_0 and α are left as free parameters while fitting the data. To find the contact point δ_0 of each force curve, the force curves are rescaled, linearised and a linear fit is performed over the first 10% of the indentation range¹³: δ_0 is the offset of indentation, which represents the point where a null force is exerted on the sample, thus it equals the point where the linear fit function intercepts the horizontal axis. The choice to fit the linearised Hertz model to the first 10% of the FC when a spherical indenter is used is supported by the observation that when $\gamma = \frac{\delta}{R} \leq 0.1$ (Figure 1c) the FCs simulated using parabolic and spherical indenters are in excellent agreement.

It is straightforward to generalise this approach to include large indentations and bottom effect corrections, or both. The correction functions $1/\Omega$ (Eq. 6,7) and $1/\Delta$ (Eq.9-12), can be integrated into the pseudo force F^* as follows¹³:

$$F_{\Omega}^* = \left(\frac{F}{\Omega}\right)^{2/3} \quad (16)$$

$$F_{\Delta}^* = \left(\frac{F}{\Delta}\right)^{2/3} \quad (17)$$

, where Eq.16 corrects for the large indentation effect, while Eq.17 corrects for the bottom effects.

In this work, we demonstrate that it is possible to combine both corrections into a single large indentations and bottom effect correction by defining the pseudo-force F^* as:

$$F_{\Delta,\Omega}^* = \left(\frac{F}{\Delta \cdot \Omega}\right)^{2/3} \quad (18)$$

The resulting pseudo-Hertzian F^* vs δ' curve (when both corrections are applied) is not affected by neither the large indentation issue, which depends on the specific geometry of the indenter (spherical vs parabolic), nor the finite thickness of the sample, and can then be fitted by the Hertz model across the whole indentation range achieved experimentally, to retrieve the correct/intrinsic YM of the specimen.

Eq.14 assumes that F^* does not depend on δ_0 , which is true when no corrections are applied. However, the functions Δ and Ω depend on δ_0 through the relation $\delta' = \delta + \delta_0$ (see Eq.16-17-18). In principle δ_0 could be considered as a free parameter to be determined through a nonlinear fit, which would cause the loss of the advantages of the linearisation. In practice, one can follow the procedure describe above for the case when no corrections are applied to determine a first estimate of δ_0 with good accuracy, then use Eq. 14,16-18 with a new indentation axis shifted by δ_0 , indicating a residual

intercept $\Delta\delta_0$ in place of δ_0 in Eq. 14. Since $\Delta\delta_0$ is typically very small compared to the maximum indentation considered in the fit, neglecting it in the definition of the independent variable of the correction functions has no tangible effect.

3.2.2. Sneddon model

If a spherical indenter is used and bottom effects are not important, the model developed by Sneddon (Eq. 3,4) can be used. This model accounts for arbitrarily large indentations, with the drawback of the lack of analytical solution. We assume here that both the measured force F' and indentation δ' contain unknown offset: $F' = F + F_0$; $\delta' = \delta + \delta_0$. Eq. 3,4 is then replaced by Eq.19,20:

$$F' - F_0 = \frac{E}{(1-\nu^2)} \left[(a^2 + R^2) \frac{(\delta' - \delta_0)}{a} - Ra \right] \quad (19)$$

$$\delta' - \delta_0 = \frac{1}{2} a \ln \left(\frac{R+a}{R-a} \right) \quad (20)$$

To obtain the YM from the experimental F' vs δ' curve, the system of Eq. 19,20 must be numerically solved, treating E , δ_0 and F_0 as free parameters. This can be done by first solving numerically Eq. 20 using an initial guess for δ_0 , to obtain the relation $a(\delta')$, then substituting a in Eq. 19 and evaluating the quadratic distance between the obtained curve and the experimental data; the best values of the free parameters E , F_0 and δ_0 are those that minimise this distance. This method is time consuming, given that typically several hundreds of force curves must be processed.

3.2.3. Linearised Sneddon model

We propose a faster method that once again takes advantage of linearisation. As for the Hertz model case, we assume that the vertical offset F_0 can be easily determined and subtracted. We then assume that the non-corrected, linearised Hertz model (Eq. 14) provides a rather accurate estimation of δ_0 when applied to the first 10% of the indentation range, i.e. far from the large indentation limit. As for the force offset, also the indentation offset can be subtracted from the indentation axis, which allows to solve numerically only once the equation:

$$\delta = \frac{1}{2} a \ln \left(\frac{R+a}{R-a} \right) \quad (21)$$

, to obtain $a(\delta)$.

We then observe that the force in Eq. 19 depends linearly on the variable s^* (with dimensions of an area) defined as:

$$s^* = \left[(a^2 + R^2) \frac{\delta}{a} - Ra \right] \quad (22)$$

, in terms of which Eq. 19 can be rewritten as:

$$F' = \frac{E}{(1-\nu^2)} s^* + \Delta F_0 \quad (23)$$

, where we have left for convenience, a residual force offset ΔF_0 . A linear regression of Eq. 23 provides the Young's modulus value.

While the standard approach, treating E , δ_0 and F_0 as free parameters in Eq. 19,20, requires a complete minimisation procedure for each FCs (the numerical inversion of Eq. 20 representing the bottleneck), the new approach requires the numerical inversion of Eq. 21, to be done only once, and then a series of linear regressions, which can be parallelise easily due to their algebraic nature, leading to a tremendous cut of computation time (the processing of a FV made of hundreds of FCs takes several minutes on a standard personal computer following the standard procedure and few seconds with the linearised one.). The free parameters ΔF_0 and E in Eq. 23 are independent, therefore a residual offset of the force does not affect the accuracy of the evaluation of the YM, assuming that δ_0 can be determined with good accuracy.

3.3 Errors analysis in FEA

Since the Hertz model is mathematically exact for a paraboloidal indenter on a flat elastic medium for arbitrarily large indentations, we assume that the discrepancy between the nominal YM (E_{nom}) and the one obtained fitting the Hertz model to the simulated force curve (E_{Hertz}) depends only on simulation-related artifacts (such as the finite mesh size) and can therefore be assumed as the smallest error that can be obtained. The error associated to the fit of the Sneddon model for the spherical indenter to the simulated curves for arbitrary indentations can be estimated in a similar way. Figure 2a shows that these errors are well below 1% across the widest range of indentations considered in this work ($0 < \delta/R < 1$).

4. RESULTS

4.1. Validation of contact mechanics models and corrections by FEA

We have used FEA to study the range of applicability of the Hertz and Sneddon model, as well as bottom effect and large indentations corrections (the three models used in the simulations are listed in Table 1). The Hertz model is exact for the paraboloidal indenter, while the Sneddon model is exact for the spherical indenter; both models, when used for the appropriate indenter geometry, are valid in principle for arbitrarily large indentations, if the material response is linearly elastic.

We performed the simulations on several ranges of indentations and calculate the Young's modulus via the Hertz and Hertz + corrections models, respectively, according to the Section 3.2. The models were fitted up to the maximum indentation achieved in each simulation. On bulk models, the simulation with the maximum indentation was equal to the tip the radius ($\delta/R = 1$); in the thin film model this was not possible, since the convergence of the solution was not accurate, and we set the simulation with the maximum indentation $\delta/R = 0.6$.

4.1.1. Hertz and Sneddon models

Artificial FCs produced simulating the B-S and B-P systems corresponding to different δ/R ratios were fitted using the Hertz, Sneddon, and Sneddon linearised models. Figure 2a shows that on B-S systems the result of the fit performed using the Sneddon model agrees within 0.7% with the nominal Young's modulus; a slightly larger maximum discrepancy (1%) is observed when the B-P system is analysed using the simple Hertz model.

Noticeably, the linearised Sneddon (Figure 2 a, purple crosses) model performs similarly, if not better, than the standard Sneddon model, across the whole range of indentations, which represents a validation of our linearised Sneddon approach. Eventually, our results confirm that when the appropriate contact mechanics model is applied with respect to the indenter geometry (i.e., Hertz model over a parabolic indenter and Sneddon model over a spherical indenter), at least for bulk films, the result is independent on the range of indentation selected for the fit, up to $\delta/R = 1$, as far as the system is linearly elastic.

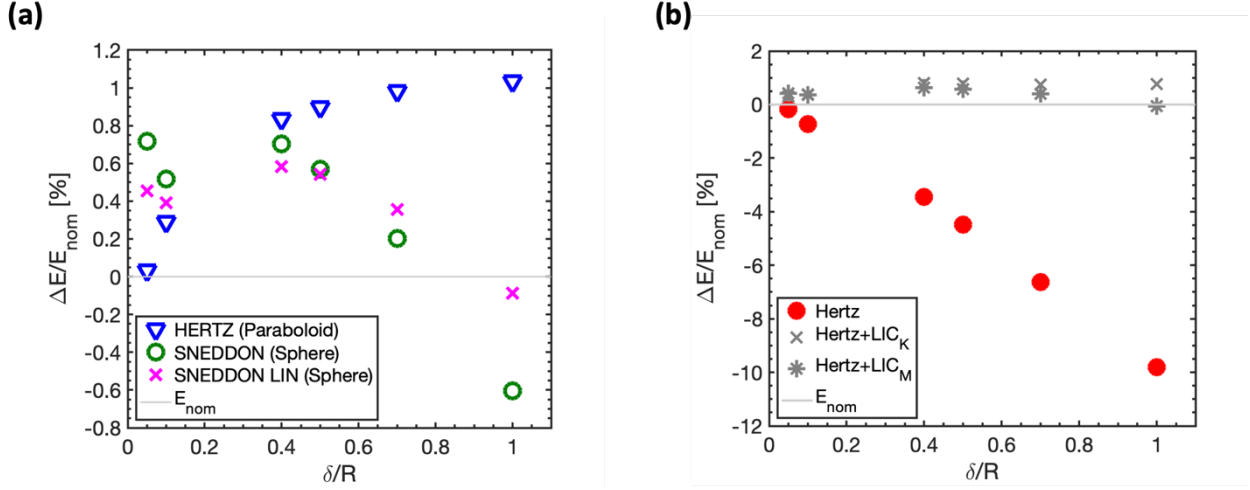


Figure 2. Relative discrepancies of the measured Young's modulus E compared to the nominal one ($E_{nom} = 0.5 \text{ MPa}$) for the bulk simulations for different ranges of indentation. The legends report the contact mechanics models used for the fit and the simulated systems (B-S and B-P) (see also Table 1). (a) Results for the appropriate matching of contact mechanics model and indenter geometry (Hertz model for the paraboloid indenter, Sneddon and linearised Sneddon models for the spherical indenter). (b) Results for the Hertz model applied to the B-S system, with and without LIC.

4.1.2. Hertz model and large indentations

The Hertz (Section 2.1) and Hertz+LIC (Section 2.3) models have been used to fit the FCs for the B-S system. The results are shown in Figure 2b. When the Hertz model is applied for indentations up to the tip radius, it underestimates the true Young's modulus of the media, with an error of approximately 10% when $\delta = R$; the error decreases almost linearly as the maximum indentation decreases, following the same trend of the LIC corrections (see Figure S2). The Hertz model, which is exact for the paraboloidal indenter, does not accurately reproduce the indentation by a spherical indenter when the condition $\delta \ll R$ is not met. The Hertz+LIC models recover the true Young's modulus within less than 1% (by default) for all indentation ranges up to $\delta = R$ (the correction proposed by Muller provides slightly more accurate results).

4.1.3. The Hertz model and simultaneous correction of bottom and large indentation effects

The effect of the spatial (vertical) confinement of the sample was explored by fitting both the simple Hertz model, the Hertz+BEC and Hertz+BEC+LIC models to the FCs simulated on the TF-S system. Films of thickness was set at $h = 2R$ and different maximum indentations δ were used to cover a wide range of χ values, up to $\chi = 0.4$ (see Section 3.3)

Figure 3a shows that as χ increases, the impact of combined large indentations and bottom effects becomes more and more pronounced, leading to a 60% overestimation of the YM for $\chi = 0.4$ ($\delta/h = 0.3$) and $\delta/R = 0.6$ (Figure 3a, simple Hertz model red circles). Noticeably, the bottom effect provides a discrepancy of 8% already at $\chi = 0.05$ ($\delta/h = 0.005$ and $\delta/R=0.01$).

To decouple large indentations and bottom effects and appreciate the overestimation of the true YM due to the vertical confinement, the FCs must be corrected first from the large indentations effect (Figure 3a, grey symbols). The effect of the large indentations when the simple Hertz model is used is to underestimate the true YM value (in any case no more than 10% at the largest χ and δ/R values); nevertheless, it is clear from our data that the bottom effect dominates the inaccuracy of the Hertz model already at moderate values of χ . Figure 2a, black symbols, shows the results of the application of the BEC only to the FCs; the true YM value is recovered with good accuracy, the residual discrepancy being due to the large indentation effect (again, with an underestimation not larger than 10% at the largest χ and δ/R values).

The result of the combined simultaneous application of large indentations and bottom effect corrections to the Hertz model is shown in Figure 3b. The maximum relative discrepancy of the measured from the nominal YM value can be further reduced to $\pm 2\%$, up to $\chi = 0.4$. According to our simulations, for $\chi < 0.32$ the residual deviation from the true YM value is comparable, in absolute terms, for Dimitriadis' and Garcia's BECs, while, for $\chi > 0.32$, Dimitriadis' formula provides better results, with an absolute deviation never exceeding 2%.

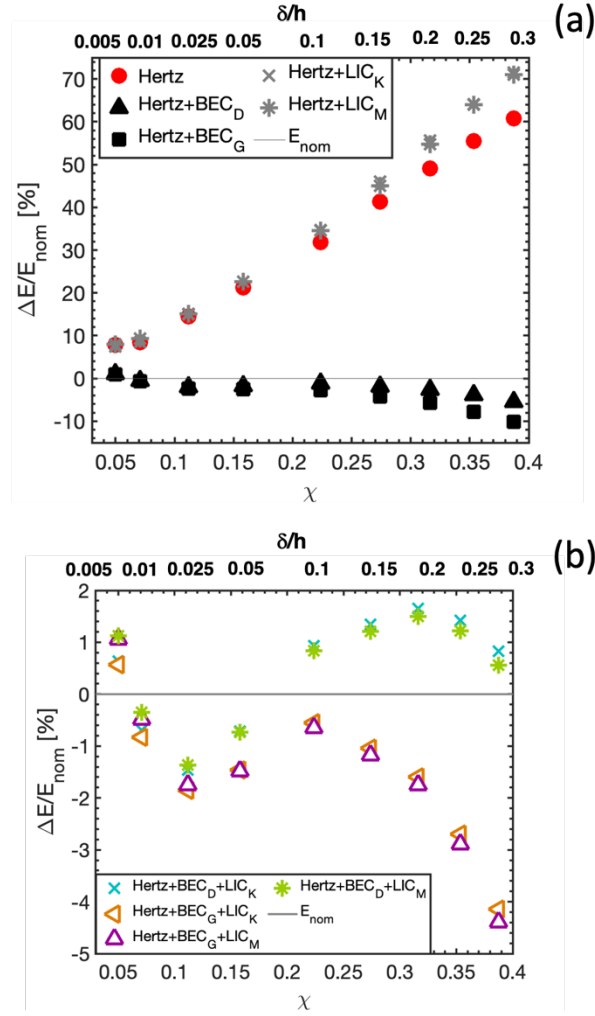


Figure 3. Relative discrepancies of the measured Young's modulus E compared to the nominal one ($E_{nom} = 0.5 \text{ MPa}$) for the TF-S system for different maximum values of the parameter $\chi = \sqrt{R\delta}/h$. (a) Results of the simple Hertzian fit, as well as of the application of the Hertz model to data corrected using only LIC or BEC. (b) The results of the combination of LIC and BEC.

Our simulations confirm that due to their multiplicative nature, the large indentations and bottom effect correction functions can be applied together to the experimental FCs obtained using a spherical indenter, to obtain sets of FCs that can be fitted using the standard Hertz model. The most accurate correction, according to our simulations, is obtained using Dimitriadis' function (Eq. 9) for the BEC and Muller's (Eq.7) for the LIC; coupling Kontomaris' correction for LIC (Eq.6) to Dimitriadis' provides only negligible worsening of the fit.

5. CONCLUSIONS

In this work, we have validated the application of Hertzian contact mechanics models and corrections in the framework of linear elasticity for the analysis of force vs indentation curves acquired using spherical probes by means of finite elements simulations. We have systematically investigated the impact of both large indentations ($\delta/R \rightarrow 1$) and vertical spatial confinement ($\chi = \sqrt{R\delta}/h \rightarrow 1$) on the accuracy of the nanomechanical analysis performed with the Hertz model.

Our results demonstrate that, on bulk systems (thick samples, for which $\chi = \sqrt{R\delta}/h \ll 1$), the standard Hertz model can be used to fit force vs indentation curves acquired using colloidal probes up to indentation $\delta \leq 0.2R$ with an error below 2%, while linearised versions of the Sneddon and Hertz+LIC models can be used to fit force curves up to $\delta = R$ maintaining the same precision. These linearised models turned out to be as accurate as the standard Sneddon model, which is computationally more demanding.

We also demonstrated that the bottom effect may lead to an overestimation of the 2% of the true YM for χ as small as 0.05. The BEC successfully restores the true YM within the 2% by default if $\delta/R < 0.2$, but when the above condition is not met, the large indentation effect leads to a more severe underestimation. We demonstrated that it is possible to combine BEC and LIC into a single correction function to apply the Hertz model to the FCs, greatly expanding its range of use and reliability, thus allowing to characterise samples possessing ample variations of thickness (height) on the scale of the tip dimensions. Such combined corrections are relevant when using micrometer-sized spherical tip in the large indentation regime (both δ/R and χ are large) and allow to take full advantage of the use of colloidal probes in the nanomechanical analysis.

The identification of reliable contact mechanics models and the standardisation of efficient and accurate data analysis methods are still open fields of investigation within the AFM and the nanoindentation community. Overall, the accurate correction of both large indentation and bottom effects can reduce the variability between results coming from different laboratories and increase the reproducibility of the nanomechanical experiments, supporting the standardisation effort.

Author contributions

Conceptualisation: MC, AP;

methodology – probe fabrication and characterisation: HH, MC, LDF;

methodology – Finite Element Simulations: LDF;

data curation and analysis HH, MC, LDF;
original draft writing and editing: MC, LDF;
draft revision: all authors;
supervision: MC, AP;
resources, funding, and project administration: AP.

Authors' contributions were allocated adopting the terminology of CRediT Contributor Roles Taxonomy.

Conflicts of interest

There are no conflicts to declare.

Acknowledgements

This research was funded by the European Union Horizon 2020 research and innovation program under the Marie Skłodowska-Curie grant agreement No. 812772, project Phys2BioMed. We thank Andrei Shvarts and Lukasz Kaczmarczyk from the University of Glasgow for support and discussions on Finite Element Simulations; we thank Ricardo Garcia from the Institute of Science and Materials of Madrid, Andreas Stylianou from the European University of Cyprus and Stylianos Vasileios Kontomaris from the Metropolitan College of Athens for useful discussions.

REFERENCES

- (1) Chighizola, M.; Dini, T.; Lenardi, C.; Milani, P.; Podestà, A.; Schulte, C. Mechanotransduction in Neuronal Cell Development and Functioning. *Biophysical Reviews*. 2019, pp 701–720. <https://doi.org/10.1007/s12551-019-00587-2>.
- (2) Takahashi, K.; Kakimoto, Y.; Toda, K.; Naruse, K. Mechanobiology in Cardiac Physiology and Diseases. *J Cell Mol Med* **2013**, *17* (2), 225–232. <https://doi.org/10.1111/jcmm.12027>.
- (3) Jackson, M. L.; Bond, A. R.; George, S. J. Mechanobiology of the Endothelium in Vascular Health and Disease: In Vitro Shear Stress Models. *Cardiovasc Drugs Ther* **2023**, *37* (5), 997–1010. <https://doi.org/10.1007/s10557-022-07385-1>.
- (4) Verbruggen, S. W.; McNamara, L. M. Bone Mechanobiology in Health and Disease. In *Mechanobiology in Health and Disease*; Elsevier, 2018; pp 157–214. <https://doi.org/10.1016/B978-0-12-812952-4.00006-4>.
- (5) Ingber, D. Mechanobiology and Diseases of Mechanotransduction. *Ann Med* **2003**, *35* (8), 564–577. <https://doi.org/10.1080/07853890310016333>.
- (6) *Mechanics of Cells and Tissues in Diseases*; Lekka, M., Navajas, D., Radmacher, M., Podestà, A., Eds.; De Gruyter, 2023.
- (7) Liu, H.; MacQueen, L. A.; Usprech, J. F.; Maleki, H.; Sider, K. L.; Doyle, M. G.; Sun, Y.; Simmons, C. A. Microdevice Arrays with Strain Sensors for 3D Mechanical Stimulation and Monitoring of Engineered Tissues. *Biomaterials* **2018**, *172*, 30–40. <https://doi.org/10.1016/j.biomaterials.2018.04.041>.
- (8) Iberite, F.; Piazzoni, M.; Guarnera, D.; Iacoponi, F.; Locarno, S.; Vannozzi, L.; Bolchi, G.; Boselli, F.; Geroges, I.; Lenardi, C.; Ricotti, L. Soft Perfusable Device to Culture Skeletal Muscle 3D Constructs in Air. *ACS Appl Bio Mater* **2023**, *6* (7), 2712–2724. <https://doi.org/10.1021/acsabm.3c00215>.
- (9) Dufrêne, Y. F.; Ando, T.; Garcia, R.; Alsteens, D.; Martinez-Martin, D.; Engel, A.; Gerber, C.; Müller, D. J. Imaging Modes of Atomic Force Microscopy for Application in Molecular and Cell Biology. *Nat Nanotechnol* **2017**, *12* (4), 295–307. <https://doi.org/10.1038/nnano.2017.45>.
- (10) MÜLLER, D. J.; DUFRÊNE, Y. F. Atomic Force Microscopy as a Multifunctional Molecular Toolbox in Nanobiotechnology. In *Nanoscience and Technology*; Co-Published with Macmillan Publishers Ltd, UK, 2009; pp 269–277. https://doi.org/10.1142/9789814287005_0028.
- (11) Holuigue, H.; Lorenc, E.; Chighizola, M.; Schulte, C.; Varinelli, L.; Deraco, M.; Guaglio, M.; Gariboldi, M.; Podestà, A. Force Sensing on Cells and Tissues by Atomic Force Microscopy. *Sensors* **2022**, *22* (6), 2197. <https://doi.org/10.3390/s22062197>.
- (12) Lorenc, E.; Holuigue, H.; Rico, F.; Podestà, A. AFM Cantilevers and Tips. In *Biomedical Methods*; De Gruyter, 2023; pp 87–104. <https://doi.org/10.1515/9783110640632-006>.
- (13) Puricelli, L.; Galluzzi, M.; Schulte, C.; Podestà, A.; Milani, P. Nanomechanical and Topographical Imaging of Living Cells by Atomic Force Microscopy with Colloidal Probes. *Review of Scientific Instruments* **2015**, *86* (3), 33705. <https://doi.org/10.1063/1.4915896>.
- (14) Indrieri, M.; Podestà, A.; Bongiorno, G.; Marchesi, D.; Milani, P. Adhesive-Free Colloidal Probes for Nanoscale Force Measurements: Production and Characterization. *Review of Scientific Instruments* **2011**, *82* (2), 023708. <https://doi.org/10.1063/1.3553499>.

- (15) Kubiak, A.; Chighizola, M.; Schulte, C.; Bryniarska, N.; Wesolowska, J.; Pudelek, M.; Lasota, M.; Ryszawy, D.; Basta-Kaim, A.; Laidler, P.; Podestà, A.; Lekka, M. Stiffening of DU145 Prostate Cancer Cells Driven by Actin Filaments-Microtubule Crosstalk Conferring Resistance to Microtubule-Targeting Drugs. *Nanoscale* **2021**, *13* (12), 6212–6226. <https://doi.org/10.1039/d0nr06464e>.
- (16) Hertz, H. Ueber Die Berührung Fester Elastischer Körper. *Journal für die Reine und Angewandte Mathematik* **1882**, *1882* (92), 156–171. <https://doi.org/10.1515/crll.1882.92.156>.
- (17) Lacaria, L.; Podestà, A.; Radmacher, M.; Rico, F. Contact Mechanics. In *Biomedical Methods*; De Gruyter, 2023; pp 21–64. <https://doi.org/10.1515/9783110640632-003>.
- (18) Dimitriadis, E. K.; Horkay, F.; Maresca, J.; Kachar, B.; Chadwick, R. S. Determination of Elastic Moduli of Thin Layers of Soft Material Using the Atomic Force Microscope. *Biophys J* **2002**, *82* (5), 2798–2810. [https://doi.org/10.1016/S0006-3495\(02\)75620-8](https://doi.org/10.1016/S0006-3495(02)75620-8).
- (19) Garcia, P. D.; Garcia, R. Determination of the Elastic Moduli of a Single Cell Cultured on a Rigid Support by Force Microscopy. *Biophys J* **2018**, *114* (12), 2923–2932. <https://doi.org/10.1016/j.bpj.2018.05.012>.
- (20) Gavara, N.; Chadwick, R. S. Determination of the Elastic Moduli of Thin Samples and Adherent Cells Using Conical Atomic Force Microscope Tips. *Nat Nanotechnol* **2012**, *7* (11), 733–736. <https://doi.org/10.1038/nnano.2012.163>.
- (21) Garcia, P. D.; Guerrero, C. R.; Garcia, R. Nanorheology of Living Cells Measured by AFM-Based Force–Distance Curves. *Nanoscale* **2020**, *12* (16), 9133–9143. <https://doi.org/10.1039/C9NR10316C>.
- (22) Kontomaris, S. V.; Malamou, A. A Novel Approximate Method to Calculate the Force Applied on an Elastic Half Space by a Rigid Sphere. *Eur J Phys* **2021**, *42* (2), 025010. <https://doi.org/10.1088/1361-6404/abccfb>.
- (23) Müller, P.; Abuhattum, S.; Möllmert, S.; Ulbricht, E.; Taubenberger, A. V.; Guck, J. Nanite: Using Machine Learning to Assess the Quality of Atomic Force Microscopy-Enabled Nano-Indentation Data. *BMC Bioinformatics* **2019**, *20* (1). <https://doi.org/10.1186/s12859-019-3010-3>.
- (24) dos Santos, Á.; Cook, A. W.; Gough, R. E.; Schilling, M.; Olszok, N. A.; Brown, I.; Wang, L.; Aaron, J.; Martin-Fernandez, M. L.; Rehfeldt, F.; Toseland, C. P. DNA Damage Alters Nuclear Mechanics through Chromatin Reorganization. *Nucleic Acids Res* **2021**, *49* (1), 340–353. <https://doi.org/10.1093/nar/gkaa1202>.
- (25) Sneddon, I. N. *The Stress on the Boundary of an Elastic Half-Plane in Which Body Forces Are Acting*; 1965; Vol. 7. <https://doi.org/10.1017/S2040618500035188>.
- (26) Long, R.; Hall, M. S.; Wu, M.; Hui, C.-Y. Effects of Gel Thickness on Microscopic Indentation Measurements of Gel Modulus. *Biophys J* **2011**, *101* (3), 643–650. <https://doi.org/10.1016/j.bpj.2011.06.049>.
- (27) Pérez-Domínguez, S.; Kulkarni, S. G.; Pabijan, J.; Gnanachandran, K.; Holuigue, H.; Eroles, M.; Lorenc, E.; Berardi, M.; Antonovaite, N.; Marini, M. L.; Lopez Alonso, J.; Redonto-Morata, L.; Dupres, V.; Janel, S.; Acharya, S.; Otero, J.; Navajas, D.; Bielawski, K.; Schillers, H.; Lafont, F.; Rico, F.; Podestà, A.; Radmacher, M.; Lekka, M. Reliable, Standardized Measurements for Cell Mechanical Properties. *Nanoscale* **2023**. <https://doi.org/10.1039/D3NR02034G>.
- (28) Schillers, H.; Rianna, C.; Schäpe, J.; Luque, T.; Doschke, H.; Wälte, M.; Uriarte, J. J.; Campillo, N.; Michanetzis, G. P. A.; Bobrowska, J.; Dumitru, A.; Herruzo, E. T.; Bovio, S.; Parot, P.; Galluzzi, M.; Podestà, A.; Puricelli, L.; Scheuring, S.; Missirlis, Y.; Garcia, R.; Odorico, M.; Teulon, J.-M.; Lafont, F.;

- Lekka, M.; Rico, F.; Rigato, A.; Pellequer, J.-L.; Oberleithner, H.; Navajas, D.; Radmacher, M. Standardized Nanomechanical Atomic Force Microscopy Procedure (SNAP) for Measuring Soft and Biological Samples. *Sci Rep* **2017**, *7* (1), 5117. <https://doi.org/10.1038/s41598-017-05383-0>.
- (29) Valero, C.; Navarro, B.; Navajas, D.; García-Aznar, J. M. Finite Element Simulation for the Mechanical Characterization of Soft Biological Materials by Atomic Force Microscopy. *J Mech Behav Biomed Mater* **2016**, *62*, 222–235. <https://doi.org/10.1016/j.jmbbm.2016.05.006>.
- (30) Lin, D. C.; Shreiber, D. I.; Dimitriadis, E. K.; Horkay, F. Spherical Indentation of Soft Matter beyond the Hertzian Regime: Numerical and Experimental Validation of Hyperelastic Models. *Biomech Model Mechanobiol* **2009**, *8* (5), 345–358. <https://doi.org/10.1007/s10237-008-0139-9>.
- (31) Wu, C. E.; Lin, K. H.; Juang, J. Y. Hertzian Load-Displacement Relation Holds for Spherical Indentation on Soft Elastic Solids Undergoing Large Deformations. *Tribol Int* **2016**, *97*, 71–76. <https://doi.org/10.1016/j.triboint.2015.12.034>.
- (32) Costa, K. D.; Yin, F. C. P. Analysis of Indentation: Implications for Measuring Mechanical Properties with Atomic Force Microscopy. *J Biomech Eng* **1999**, *121* (5), 462–471. <https://doi.org/10.1115/1.2835074>.
- (33) Kontomaris, S. V.; Stylianou, A.; Georgakopoulos, A.; Malamou, A. Is It Mathematically Correct to Fit AFM Data (Obtained on Biological Materials) to Equations Arising from Hertzian Mechanics? *Micron* **2023**, *164*, 103384. <https://doi.org/10.1016/j.micron.2022.103384>.
- (34) Kontomaris, S. V.; Malamou, A. Hertz Model or Oliver & Pharr Analysis? Tutorial Regarding AFM Nanoindentation Experiments on Biological Samples. *Mater Res Express* **2020**, *7* (3), 033001. <https://doi.org/10.1088/2053-1591/ab79ce>.
- (35) Kontomaris, S.-V.; Malamou, A. Revisiting the Theory behind AFM Indentation Procedures. Exploring the Physical Significance of Fundamental Equations. *Eur J Phys* **2022**, *43* (1), 015010. <https://doi.org/10.1088/1361-6404/ac3674>.
- (36) Fischer-Cripps, A. C. *The Hertzian Contact Surface*; 1999; Vol. 34, pp 129–137. <https://doi.org/10.1023/A:1004490230078>.
- (37) Sneddon, I. N. The Relation between Load and Penetration in the Axisymmetric Boussinesq Problem for a Punch of Arbitrary Profile. *Int J Eng Sci* **1965**, *3* (1), 47–57. [https://doi.org/10.1016/0020-7225\(65\)90019-4](https://doi.org/10.1016/0020-7225(65)90019-4).
- (38) Park, K.-B.; Kim, M.-S.; Kim, J.-H.; Kim, S.-K.; Lee, J.-M. Analysis of the Mechanical Properties of Polymer Materials Considering Lateral Confinement Effects. *Journal of Polymer Engineering* **2019**, *39* (5), 432–441. <https://doi.org/10.1515/polyeng-2018-0299>.
- (39) Landau, L. D. (Lev D.); Lifshits, E. M. (Evgenii M.); Kosevich, A. Markovich.; Pitaevskii, L. P. (Lev P. Theory of Elasticity. **1986**, 187.
- (40) Wu, C.-E.; Lin, K.-H.; Juang, J.-Y. Hertzian Load–Displacement Relation Holds for Spherical Indentation on Soft Elastic Solids Undergoing Large Deformations. *Tribol Int* **2016**, *97*, 71–76. <https://doi.org/10.1016/j.triboint.2015.12.034>.
- (41) Carl, P.; Schillers, H. Elasticity Measurement of Living Cells with an Atomic Force Microscope: Data Acquisition and Processing. *Pflugers Arch* **2008**, *457* (2), 551–559. <https://doi.org/10.1007/S00424-008-0524-3>.

Validation of contact mechanics models for Atomic Force Microscopy via Finite Elements Analysis

L. Dal Fabbro, H. Holuigue, M. Chighizola* and A. Podestà*

Dipartimento di Fisica "Aldo Pontremoli" and CIMaINa, Università degli Studi di Milano,
via G. Celoria 16, 20133, Milano, Italy.

*Corresponding authors. E-mail: matteo.chighizola@unimi.it, alessandro.podesta@unimi.it

SUPPLEMENTARY INFORMATION

Table of Contents

<i>Figure S1. Evolution of the contact radius a with the δ/R ratio.....</i>	2
<i>Figure S2. Absolute values of the Hertz model correction functions $\Omega(\gamma)$ and $\Delta(\chi)$.....</i>	2
<i>Figure S3. Effective stress vs effective strain</i>	3
<i>Figure S4. Young's modulus ratio E/E_{nom} measured from linearized force curves simulated with the Bulk-Sphere model.....</i>	3

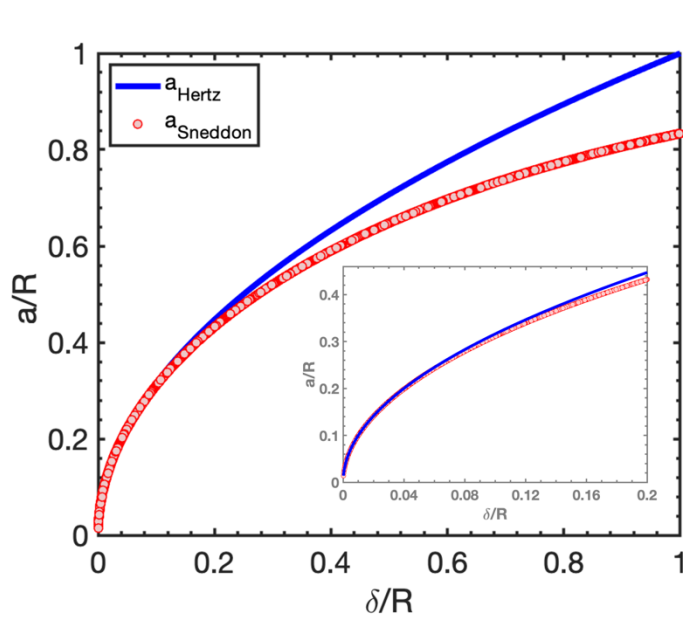


Figure S1. Evolution of the contact radius a with the δ/R ratio, for two geometries of the indenter: Paraboloid on Bulk (a_{Hertz}) and Sphere on Bulk ($a_{Sneddon}$). The inset shows an expanded view of the small δ/R values region.

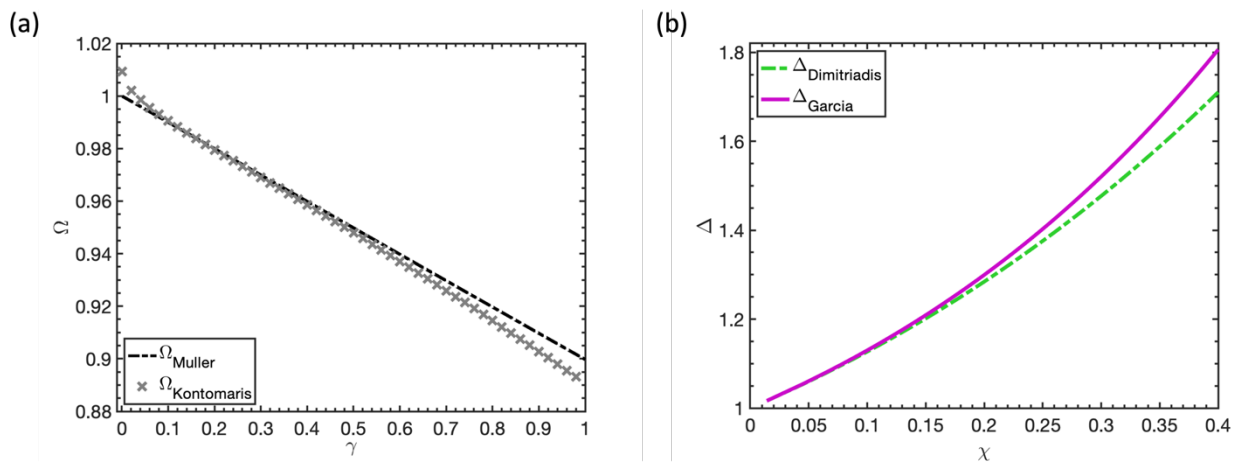


Figure S2. Absolute values of the Hertz model correction functions $\Omega(\gamma)$ and $\Delta(\chi)$ ($\gamma = \delta/R$, $\chi = a/h$) for a bonded sample in the explored ranges of the parameters. (a) LIC, and (b) BEC functions.

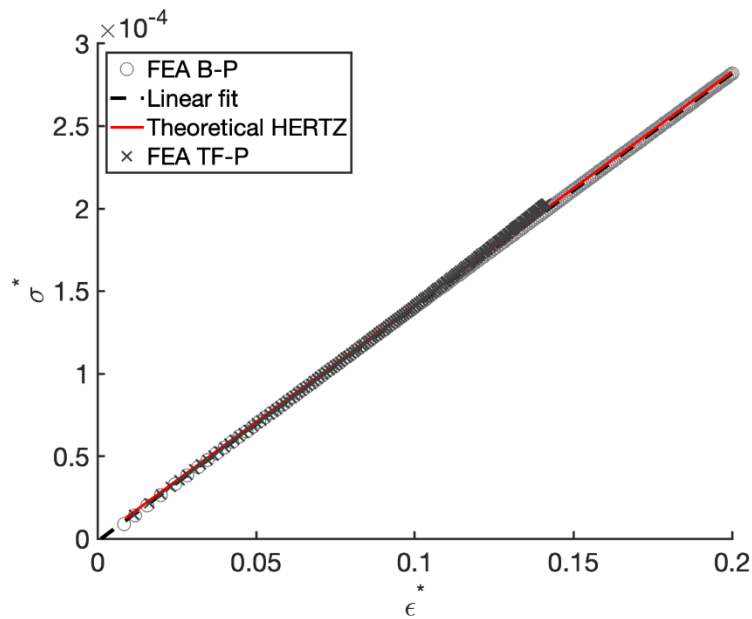


Figure S3. Effective stress vs effective strain (calculated using the Tabor's relations¹) for the Bulk-Paraboloid (B-P) and Thin Film-Paraboloid (TF-P) configurations simulated with ANSYS software with the large deformations option enabled.

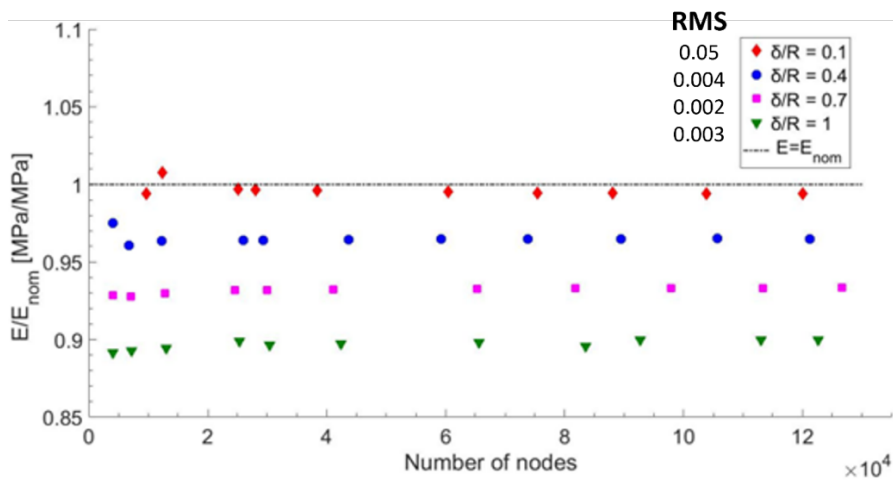


Figure S4. Young's modulus ratio E/E_{nom} measured from linearized force curves simulated with the Bulk-Sphere model. E is the Young's modulus obtained from the linear fit, $E_{nom} = 0.5 \text{ MPa}$ is the nominal value used in the simulations. As the δ/R ratio increases and the contact departs from the hertzian model (large indentation effect), the Young's modulus decreases, irrespective of the number of nodes. The dashed line refers to the ideal hertzian contact. The root mean square (RMS) values of each series are reported.

- (1) Lin, D. C.; Shreiber, D. I.; Dimitriadis, E. K.; Horkay, F. Spherical Indentation of Soft Matter beyond the Hertzian Regime: Numerical and Experimental Validation of Hyperelastic Models. *Biomech Model Mechanobiol* **2009**, *8* (5), 345–358. <https://doi.org/10.1007/s10237-008-0139-9>.